

CHANDRA OBSERVATIONS OF THE GALAXY CLUSTER A478: THE INTERACTION OF HOT GAS AND RADIO PLASMA IN THE CORE, AND AN IMPROVED DETERMINATION OF THE COMPTON γ -PARAMETER

M. SUN,¹ C. JONES,¹ S. S. MURRAY,¹ S. W. ALLEN,² A. C. FABIAN,² AND A. C. EDGE³

Received 2002 August 14; accepted 2003 January 2

ABSTRACT

We present the results from a 42 ks *Chandra* ACIS observation of the galaxy cluster A478. This cluster is generally considered to be highly relaxed. The *Chandra* image reveals, for the first time, X-ray cavities in the hot gas within the central 15 kpc radius of A478. Two weak and small (~ 4 kpc) radio lobes that extend from the central nucleus are detected in a 1.4 GHz VLA observation. The radio lobes are roughly along the direction of the X-ray cavities, but are much smaller than the X-ray cavities. We propose a “doughnut” configuration for the hot gas within the central 15 kpc, created by the interaction of the gas with the radio plasma that originated from the nucleus. The current radio activity of the central radio source is weak ($\sim 0.2\%$ of Hydra A) and the total radio power is at least 10 times smaller than the minimum power needed to create the cavities. We compare A478 with other galaxy clusters in which similar X-ray cavities were found. A478 and A4059 host much weaker central radio sources than do others with similarly sized X-ray cavities. On larger scales, deprojected temperature and density profiles are obtained for A478. We used these to derive the Compton γ -parameter, for the first time, through direct integration. The result has a much smaller statistical uncertainty than previous ones. This serves as an example of how high-quality X-ray data can help constrain H_0 . The corresponding H_0 also was derived combining the available Sunyaev-Zeldovich effect measurement.

Subject headings: distance scale — galaxies: clusters: individual (A478) — radio continuum: galaxies — X-rays: galaxies: clusters

1. INTRODUCTION

A478 is an X-ray-luminous cluster at a redshift of 0.088 (Zabludoff, Huchra, & Geller 1990). Previous X-ray observations with *Ginga*, *Einstein*, and *ROSAT* suggested that it contains one of the largest central cooling flows with estimates up to $\sim 1000 M_\odot \text{ yr}^{-1}$ (Johnstone et al. 1992; Allen et al. 1993; White et al. 1994; Allen 2000). These observations also indicated excess X-ray absorption above the Galactic value. The X-ray morphology of A478 implies it is a very relaxed cluster (e.g., Allen et al. 1993), although it is elongated in the northeast-southwest direction (e.g., White et al. 1994). This elongation is along the same direction as the cluster galaxies (Bahcall & Sargent 1977), as well as the light distribution of the cD galaxy (White et al. 1994). A478 also has a marginal CO detection of $(4.5 \pm 2.2) \times 10^9 M_\odot$ (Edge 2001). A strong Sunyaev-Zeldovich (SZE) decrement is detected in this cluster, making it an excellent target to measure the Hubble constant (Myers et al. 1997, hereafter M97; Mason, Myers, & Readhead 2001, hereafter M01).

In this paper, we present initial results from a recent *Chandra* 42 ks ACIS observation of A478, with emphasis on the central X-ray gas/radio source interaction and an improved result for the predicted Compton γ -parameter using the temperature and density profiles measured with *Chandra*. A detailed analysis of the cooling flow will be presented in another paper. Throughout this paper we assume $H_0 = 70 \text{ km s}^{-1} \text{ Mpc}^{-1}$, $\Omega_M = 0.3$, and $\Omega_\Lambda = 0.7$ unless

specified. At a redshift of 0.088, the luminosity distance to A478 is 403 Mpc, and $1'' = 1.65 \text{ kpc}$.

2. CHANDRA OBSERVATION AND DATA REDUCTION

A478 was observed for 42.4 ks on 2001 January 29 by *Chandra* with the Advanced CCD Imaging Spectrometer (ACIS). The observation used CCDs I2–I3 and S1–S4 with the cluster centered on S3. The data were telemetered in Faint mode, and *ASCA* grades 1, 5, and 7 were excluded. Known bad columns, hot pixels, and CCD node boundaries also were excluded. We investigated the background light curves from the back-illuminated (BI) S1 CCD and from the front-illuminated (FI) CCDs, using the standard software.⁴ No background flares were found in this observation. The streak events in the S4 CCD were removed by CIAO DESTREAK software.

In our analysis we used period D blank-field background data by M. Markevitch.⁵ The particle background level was measured in the hard band (7–11 keV) for the S1 CCD (far from the cluster) and in PHA channels 2500–3000 ADU for all CCDs. We found that the particle background level was 10% lower than that of the period D background data. This is within the uncertainties for the background files. Moreover, the observation was taken at the time that S3 background rate was the lowest.⁶ Thus, we decreased the background normalization by 10% to fit the particle background level at the

¹ Harvard-Smithsonian Center for Astrophysics, 60 Garden Street, Cambridge, MA 02138; msun@cfa.harvard.edu.

² Institute of Astronomy, Madingley Road, Cambridge CB3 0HA, UK.

³ Department of Physics, University of Durham, South Road, Durham DH1 3LE, UK.

⁴ <http://cxc.harvard.edu/contrib/maxim/bg/index.html>.

⁵ <http://cxc.harvard.edu/contrib/maxim/acisbg>.

⁶ http://cxc.harvard.edu/ccw/proceedings/presentations/m_markevitch/pg002.html.

time of the A478 observation as recommended in Markevitch et al. (2003). This correction has only a small effect on the best-fit temperature (e.g., 10% for the outermost annulus in § 4). Note that although the correction should apply only to the particle component of the total background and not to the cosmic X-ray background (CXB), the particle component is dominant at energies greater than ~ 3 keV, which are most important for measuring the gas temperature. This small rescaling of the CXB component has little effect on the spectral fitting (e.g., $\sim 5\%$ for the outermost annulus). We also corrected for the readout effect in the S3 CCD caused by the bright cluster core (see Markevitch et al. 2000 for details). Two corrections were made to the ACIS low-energy quantum efficiency (QE). The first uses CXC (*Chandra* X-ray Center) contributed software to correct for the QE degradation⁷ (Plucinsky et al. 2003). The second corrects the QE by an empirical factor of 0.93 below 1.8 keV in the FI CCDs to improve the cross-calibration with the BI CCDs⁸ (also see Markevitch & Vikhlinin 2001 for details). The tools “calcrmf” and “calcarf” by Vikhlinin were used to generate response files.

The calibration files used correspond to CALDB 2.15 from the CXC. The uncertainties quoted in this paper are 90% confidence intervals unless specified. The solar abundance table by Anders & Grevesse (1989) and a cluster redshift of 0.088 were used in the spectral fits and computations.

⁷ http://cxc.harvard.edu/cal/Links/Acis/acis/Cal_prods/qeDeg/index.html.

⁸ http://asc.harvard.edu/cal/Links/Acis/acis/Cal_prods/qe/12_01_00/.

3. CENTRAL REGION OF A478

On large scales from 50 kpc to several Mpc, A478 appears quite relaxed, although the X-ray morphology is elliptical rather than circular (Fig. 1a). The superior angular resolution of *Chandra* allows us to examine structures on scales of several kpc at the center of A478. In the central 20 kpc (Fig. 1b), the cluster shows significant structures. The X-ray emission appears double-peaked (separated by ~ 8 kpc), with the two peaks lying east and west of the cD galaxy nucleus. In contrast to the double peaks, there are depressions north and south of the cD nucleus. To better quantitatively show the depressions, we measured the surface brightness profiles in four directions from the nucleus within ~ 15 kpc (Fig. 2). The surface brightness in the north and south sectors is 20%–30% lower than that to the west and east. Beyond ~ 20 kpc, no significant difference between the surface brightness of the sectors is seen. Since the X-ray depressions seen in A478 are similar to the X-ray cavities observed in other clusters (e.g., Hydra A, McNamara et al. 2000) where central radio sources are certainly responsible, we investigated the radio activity of the central source in A478.

A 1.4 GHz VLA image of A478, obtained in 630 s with the A array on 1998 March 1, is shown as iso-intensity contours in Figure 1b. The central radio source is composed of a bright pointlike source at the position of the cD nucleus, with weak extensions (lobes) toward the northeast and southwest. The measured 1.4 GHz total flux is about 30 mJy, with the lobes contributing $\sim 35\%$ of this. The radio lobes are quite small: ~ 4 –5 kpc extension for the southwest one and ~ 3 –4 kpc extension for the northeast one (the VLA angular resolution at 1.4 GHz is $1''.5$, or 2.5 kpc). They lie roughly along the direction of the X-ray depressions,

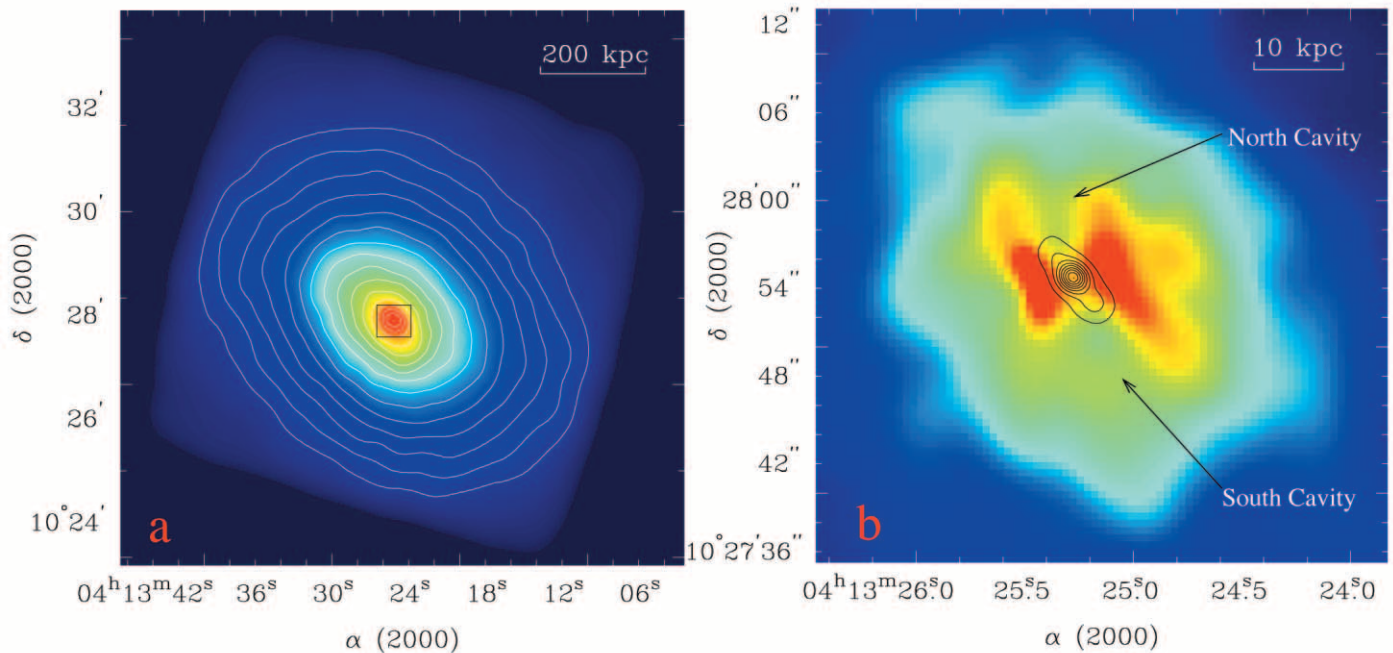


FIG. 1.—(a) *Chandra* ACIS-S3 0.5–5 keV image of A478 (background subtracted and exposure corrected) with iso-intensity contours superposed. The source was centered on S3 CCD. The contour levels increase by a factor of $\sqrt{2}$ from the outermost one (0.039 counts s^{-1} arcmin $^{-2}$). The image has been smoothed by Gaussians with variable σ , ranging from $3''$ at the center to $20''$ at the outskirts. The small box at the center is the region shown on the right. (b) Adaptively smoothed *Chandra* 0.5–5 keV image of the central part of A478 (represented by the small box in the left image) with 1.4 GHz radio contours superposed. The *Chandra* image was smoothed to 3 – 4 σ significance by CSMOOTH in CIAO. The color scale is linear and ranges from 3.0×10^{-4} to 2.5×10^{-3} counts s^{-1} arcsec $^{-2}$. The radio contours are in linear scale. The beam size of the radio observation is $1''.5$. The two X-ray cavities are clear and labeled.

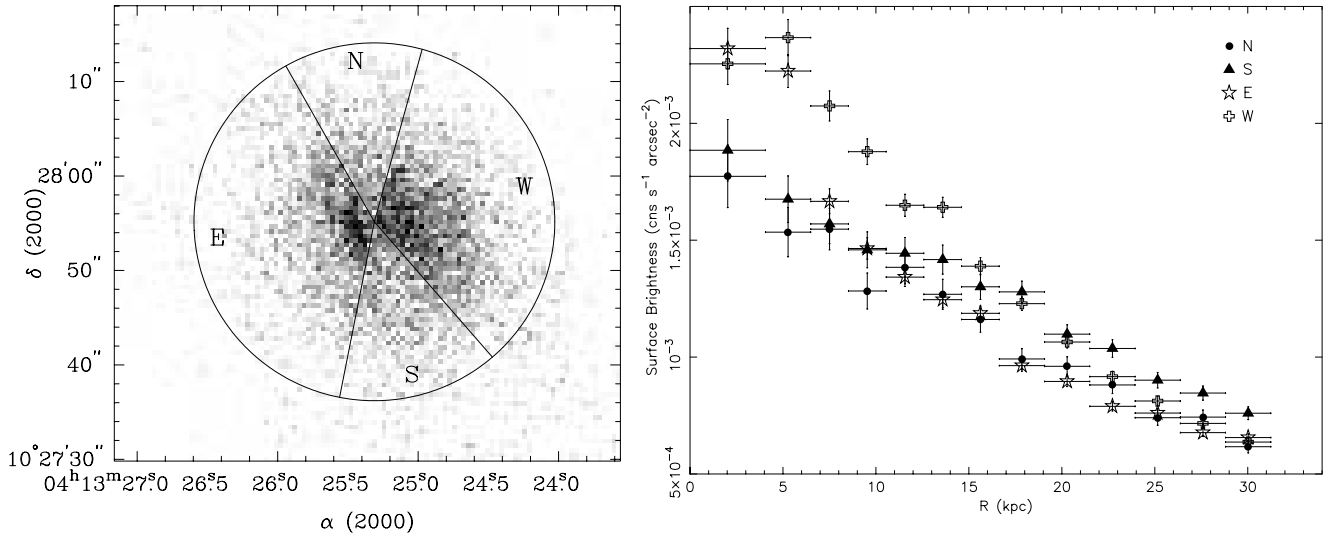


FIG. 2.—*Left*: 0.5–5 keV photon image of the central part. The four regions used to measure surface brightness profiles are shown. *Right*: Surface brightness profiles in four directions within the inner 30 kpc. The depressions south and north of the center are significant. The western peak is more extended than the eastern one.

although the X-ray depressions are much larger than the detected radio lobes. The two X-ray peaks are located along the east and west sides of the radio source. The correspondence of radio lobes and X-ray structure suggests that the X-ray structure was created by the interaction of the hot gas with the radio lobes. Similar X-ray structures (X-ray cavities) have been found at the centers of a number of cooling flow clusters (Hydra A—McNamara et al. 2000; Perseus Cluster—Boehringer et al. 1993, Fabian et al. 2000; A2052—Blanton et al. 2001; A2597—McNamara et al. 2001; A4059—Heinz et al. 2002). Generally, they are thought to form when the hot gas is displaced by the expansion of radio lobes or rising buoyant bubbles (e.g., Churazov et al. 2001; Soker, Blanton, & Sarazin 2002). For consistency, hereafter we also call the X-ray structures in A478 cavities.

No X-ray point source is detected at the position of the nucleus of the cD galaxy, where a radio point source is detected (Fig. 1*b*). Assuming a $\Gamma = 1.7$ power law modified by an absorption of $2.6 \times 10^{21} \text{ cm}^{-2}$ (the best fit, see § 4) and a cluster redshift of 0.088, the 3σ upper limit on the point source luminosity is $3 \times 10^{41} \text{ ergs s}^{-1}$ (0.5–10 keV). If the central source is as highly obscured as the one in Hydra A (McNamara et al. 2000), the upper limit will be higher (e.g., $1.1 \times 10^{42} \text{ ergs s}^{-1}$ for $N_{\text{H}} = 2.6 \times 10^{22} \text{ cm}^{-2}$, which is comparable to the source detected in Hydra A).

Spectra of the two X-ray peaks were extracted from $10''$ (major axis) \times $4''$ (minor axis) ellipses centered on them. We fitted each with a MEKAL model and found consistent temperatures and abundances: $3.2 \pm 0.2 \text{ keV}$ and $0.60^{+0.20}_{-0.17}$ for the eastern peak, $3.1 \pm 0.2 \text{ keV}$ and $0.65^{+0.21}_{-0.18}$ for the western peak. A map of the hardness ratio (2–5 keV/0.5–2 keV) for the central $60 \text{ kpc} \times 60 \text{ kpc}$ region is shown in Figure 3. The coolest region contains the two peaks and regions between them. The overall temperature increases outward from the core. There is no indication at shock heated regions around the X-ray cavities. The spectrum of the central 20 kpc (radius) region was fit with a MEKAL + MKCFLOW

model to search for any cooling flow component. The inclusion of a cooling flow model (MKCFLOW) did not significantly improve the fit if we allow the gas to cool to zero. However, if we use a lower temperature limit of $\sim 1 \text{ keV}$, the fit improves significantly. Thus, while there is a clear signature of gas cooling toward the center (see § 4), the spectral fits do not require gas at very low temperatures.

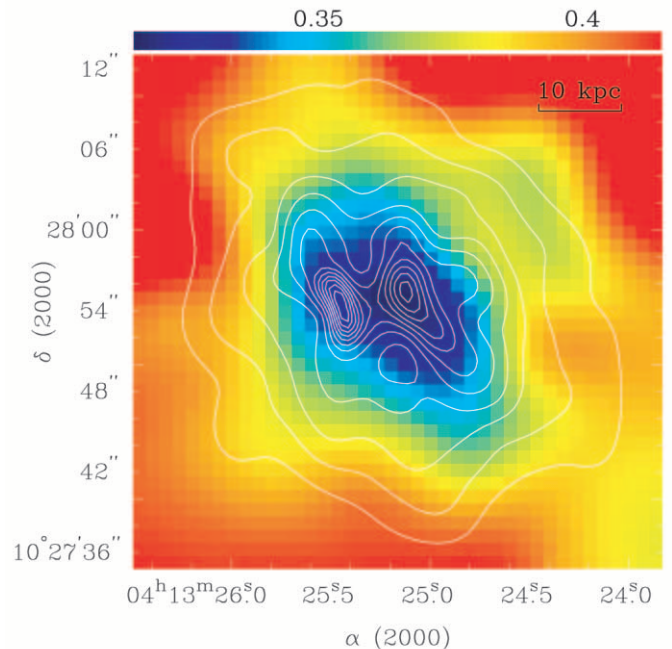


FIG. 3.—Hardness ratio map of the central region of A478 (the same region as Fig. 1*b*) superposed on the X-ray contours (in linear scale). The hardness ratio is defined as (2.0–5.0 keV)/(0.5–2.0 keV). Thus, the lower the value is, the cooler the temperature is. The typical statistical uncertainty of the hardness ratio ranges from ~ 0.02 at the center to ~ 0.03 near the edge of the field. Using the overall absorption value for A478, a hardness ratio of 0.32 is expected for a gas with a 3.5 keV temperature, while gas at 5.5 keV would produce a hardness ratio of 0.41.

4. ANALYSIS OF THE TEMPERATURE, ABSORPTION, AND HEAVY-ELEMENT ABUNDANCE PROFILES

We first compare the integrated spectrum of A478 from the entire S2, S3, and S4 CCDs with previous results. Data in the 0.7–8 keV energy band are used. The results are $N_{\text{H}} = (0.259 \pm 0.003) \times 10^{22} \text{ cm}^{-2}$, $T = 7.18 \pm 0.11 \text{ keV}$, and abundance 0.37 ± 0.02 solar. From *ASCA* GIS 1–9 keV data, White (2000) obtained a temperature of $6.6 \pm 0.4 \text{ keV}$ and an abundance of 0.31 ± 0.05 with a fixed absorption of $3 \times 10^{21} \text{ cm}^{-2}$. If we fix the absorption at their value, we find a consistent temperature $T = 6.62 \pm 0.09 \text{ keV}$ and an abundance of 0.37 ± 0.02 .

Although in X-rays A478 is somewhat elliptical, it is useful to derive radial properties of the temperature, absorption, and heavy-element abundance. For the profiles, we centered all annuli at R.A. $04^{\text{h}}13^{\text{m}}25^{\text{s}}.3$, decl. $10^{\circ}27'53''$ and required each annulus to contain 6000–8000 source counts. Each annulus was fitted by a MEKAL model, with the absorption, temperature, and abundance as free parameters. The reduced χ^2 ranged from 0.8 to 1.4, and most were around 1.0 (for 125–245 degrees of freedom), which is acceptable considering the large number of source counts and the current ACIS calibration. The derived temperature profile is shown in Figure 4. The temperature falls from $\sim 8.5 \text{ keV}$ at large radii to $\sim 3 \text{ keV}$ at the center. Between radii of ~ 110 and $\sim 500 \text{ kpc}$, gas temperatures are consistent with a constant temperature of $\sim 8.5 \text{ keV}$. To better constrain the absorption and abundance, we used larger radial bins and obtained the results shown in Figure 5. The abundance increases from ~ 0.3 solar at several hundred kiloparsecs to ~ 0.6 solar at the center. The absorption also increases toward the center. The spectra in the regions outside $\sim 500 \text{ kpc}$ (in CCDs S2, S4, I2, and I3) were fitted

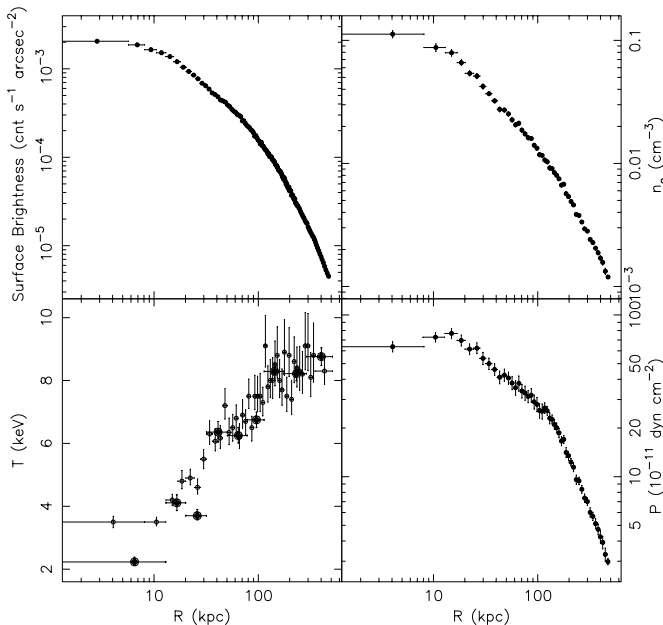


FIG. 4.—Surface brightness (0.5–5 keV) (upper left), electron density (upper right), temperature (lower left), and pressure (lower right), as functions of radius. Only statistical uncertainties are shown (1σ random errors). In the temperature profile, the data points with small circles are projected temperatures, while the data points with large filled circles are deprojected temperatures. To derive the pressure profile, we use the power-law fit of the temperature profile.

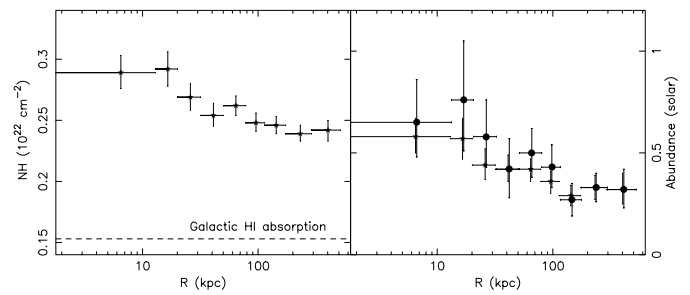


FIG. 5.—Left: The best-fit N_{H} with 90% uncertainties in nine radial bins to $\sim 500 \text{ kpc}$. The dashed line is the Galactic H I absorption ($1.53 \times 10^{21} \text{ cm}^{-2}$). The observed absorption is significantly higher than that value and peaks at the center. Right: The measured abundance with 90% uncertainties for each radial bin. The data points with stars are projected abundances, while the data points with large filled circle are deprojected abundances. The radial positions of the deprojected abundances are shifted a little bit to allow the error bars to be better seen.

simultaneously with a fixed absorption of $0.24 \times 10^{22} \text{ cm}^{-2}$ (extrapolated from the absorption profile shown in Fig. 5). The best-fit temperature is $6.45^{+0.80}_{-0.75} \text{ keV}$ and will be taken as the “background” temperature in the deprojection analysis (§ 5).

5. DEPROJECTION ANALYSIS

Although the X-ray morphology of A478 is elliptical rather than circular, the ellipticity is small (~ 0.2) and a spherical approximation serves as a simple way to do the deprojection and other analyses. Thus, on the basis of the two-dimensional temperature profile obtained in § 4, we performed a deprojection analysis to obtain the three-dimensional temperature profile and abundance profile (see e.g., David et al. 2001 for details of the spectral deprojection). Nine radial bins were chosen for the spectral deprojection. These were the same ones used above to derive the absorption and abundance profiles. To account simply for the slight decrease of absorption with radius, we used two absorption values, $0.28 \times 10^{22} \text{ cm}^{-2}$ for annuli 1–3 and $0.25 \times 10^{22} \text{ cm}^{-2}$ for annuli 4–9 (Fig. 5), derived by fitting a single absorption for these regions ($\chi^2 = 8.1/7$). The deprojection result is shown in Figure 4. For regions within a radius of $\sim 110 \text{ kpc}$, we also fitted the three-dimensional temperatures with a power law given by $T(r) = T_0(r/10 \text{ kpc})^\alpha$. The best fit is $T_0 = 2.79 \pm 0.09 \text{ keV}$ and $\alpha = 0.412 \pm 0.017$ (1σ errors). Deprojected abundances are shown in Figure 5.

The surface brightness profile of A478 is shown in Figure 4. There is at least one inflection point at $\sim 40 \text{ kpc}$. If the surface brightness profile is fitted by a single- β model, the central excess is quite significant, and the fit is poor. Thus, we use a deprojection technique to determine the electron density profile rather than fitting with a multivariate function (see a recent example in David et al. 2001). This technique converts the observed surface brightness to the electron density starting in the largest annulus and then determines the density at progressively smaller radii, after removing the projected emission from larger radii. The fraction of cluster emission in all radial bins arising from gas outside the outermost annulus ($\sim 5'$ radius) is corrected using the power-law fit to both *Chandra* and *PSPC* surface brightness profiles in regions outside the outermost annulus. The deprojected temperature and abundance profiles were combined to

produce an emissivity profile (with uncertainties) used in the conversion. We performed 400 Monte Carlo simulations to estimate the errors.

The deprojected electron density profile is shown in Figure 4, as well as the pressure profile. The density profile gradually steepens from $n_e \propto r^{-0.25}$ at 10 kpc to $n_e \propto r^{-1.65}$ at 250 kpc, and there is no flat density core. The isobaric cooling time is 4×10^8 yr in the innermost 10 kpc and less than a Hubble time ($\sim 10^{10}$ yr) within the central 140 kpc. The pressure reaches a maximum at $r \sim 15$ kpc, at roughly the outer edge of the X-ray cavities.

6. DISCUSSION

6.1. Central X-Ray Gas/Radio Source Interaction

As shown in § 3, there are two X-ray cavities in A478. The alignment of the radio lobes and X-ray cavities implies that the X-ray gas was swept out of the cavities by expanding radio plasma. We suggest that the X-ray double peaks result from a “doughnut” configuration of the hot gas around the central nucleus, with the plane of the “doughnut” perpendicular to the direction of the radio lobes, while the central parts of the “doughnut” were displaced by the expanding radio plasma. The absence of shocked regions in the A478 core (Fig. 3) is consistent with the radio plasma expanding subsonically, which is similar to what was found in other clusters (e.g., Hydra A and Perseus). If we assume the X-ray cavities are shaped like circular cones, the minimum energy required to sweep the gas out of the current cavities is $pV \simeq 3 \times 10^{58}$ ergs. Churazov et al. (2001) showed that a large and strongly underdense bubble will rise with a velocity comparable to the Keplerian velocity. Therefore, as a first-order approximation, we take the Keplerian velocity at 10 kpc to represent the rising velocity of the bubble (~ 460 km s^{-1} ; the mass is estimated from the deprojected temperature and density under the assumption of hydrostatic equilibrium). Thus, the time to form the current cavities is $\sim 3 \times 10^7$ yr. Therefore, the minimum average power from the central source to create the X-ray cavities is $\sim 3 \times 10^{43}$ ergs s^{-1} , which is at least 10 times larger than the current total radio power from the central source. Since the total radio power is simply a lower limit to the kinetic power of the jet (e.g., Perseus—Fabian et al. 2002), more radio information is required to conclude whether the current kinetic power of the jet could create the X-ray cavities. However, the observed radio lobes are considerably smaller than the X-ray cavities, which may imply a fading of the radio source within $\sim 10^7$ – 10^8 yr.

Five other clusters also contain X-ray cavities. Although each is very complicated, in Figure 6 we compare the cavity size and the 1.4 GHz luminosity of the central radio source for all of them. Although the kinetic power of the radio source is generally unknown, Heinz et al. (2002) argued that the upper limit on the current kinetic power was proportional to the current 1.4 GHz luminosity. In A478 the 1.4 GHz luminosity of the central source is the smallest in this sample (less than 7% of any others) and the radio lobes are the smallest. Thus, A478 serves as an important example for understanding X-ray gas/radio plasma interaction in the center of cooling-flow clusters. The size of the X-ray cavities in A478 are $\sim \frac{3}{4}$ the size of those in Perseus (Fig. 6), but their 1.4 GHz luminosities differ by ~ 20 . In Figure 6, if we use the three clusters in which the central radio sources are power-

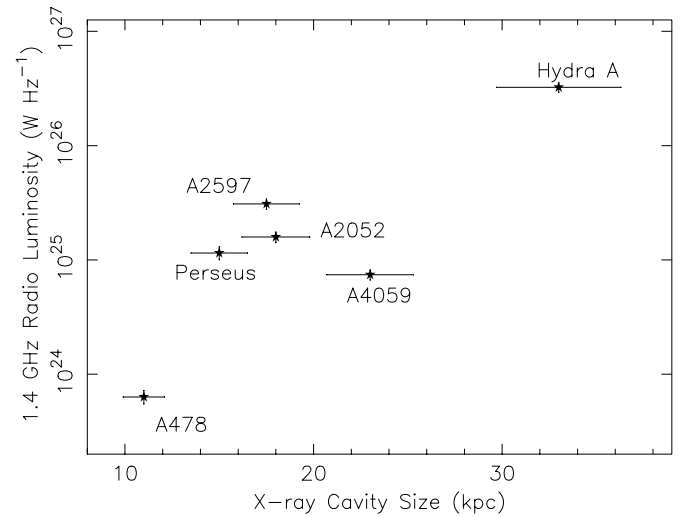


FIG. 6.—X-ray cavity size vs. 1.4 GHz luminosity of the cD galaxy for clusters with X-ray cavities detected. For each cluster, we plot the larger cavity size. The cavity sizes are measured by eye, and 10% errors are also shown. The 1.4 GHz luminosities for clusters were obtained from A478 (our measurement), A2052 (Zhao et al. 1993), A4059 (Heinz et al. 2002), A2597 (McNamara et al. 2001), Hydra A (Ekers & Simkin 1983), and Perseus (Fabian et al. 2000).

ful enough to create the X-ray cavities (Hydra A, A2052, and Perseus) to define a line, A478 and A4059 have much lower 1.4 GHz luminosities ($\sim 10\%$) than the values predicted by that line. Heinz et al. (2002) suggested that the central radio source in A4059 had faded by about an order of magnitude on a timescale less than 10^8 yr, since the current kinetic power they estimated is too small to create the X-ray cavities. If we adopt their method, A478 is very similar to A4059: in both clusters, the estimated current kinetic power is too small to create the X-ray cavities. Thus, A478 and A4059 may be in a different “phase” of their active nuclei cycles than the other sources.

6.2. An Improved Estimation of the Compton y -Parameter

To date, X-ray observations have been combined with SZE measurements to estimate H_0 for over 20 galaxy clusters (e.g., M97; Hughes & Birkinshaw 1998; Reese et al. 2000; Mauskopf et al. 2000). However, these analyses generally used only single temperatures (or simple temperature profiles) and density profiles derived by simple β models. These can introduce significant errors in some cases, such as for cooling flow clusters in which a single- β model usually fails to describe the central region, or clusters with significant temperature gradients (Hughes & Birkinshaw 1998). It is ideal and more accurate to apply directly the observed density and temperature profiles to models. In this paper, for the first time, we apply the deprojected density and temperature profiles and use direct integration to derive the Compton y -parameter

$$y = \frac{k\sigma_T}{m_e c^2} \int_{-\infty}^{\infty} T_e n_e d\zeta. \quad (1)$$

In this section, we use $H_0 = 100 h$ km s^{-1} Mpc $^{-1}$ and assume spherical symmetry of the cluster X-ray emission. In § 5, we derived the deprojected density profile within the inner $5'$ (Fig. 4). For the outer regions, we combined *Chandra* and *ROSAT* PSPC images and fitted the surface

brightness profile with a β model. The derived parameters are $\beta = 0.68 \pm 0.01$ and core radius $r_0 = 1'02 \pm 0'07$ (1σ errors). The density profile beyond $5'$ was obtained from this β model. Combining the deprojected density profile with the deprojected temperature profiles $[n_e(r)$ and $T_e(r)$ in § 5], the Compton y -parameters can be computed for different lines of sight. The uncertainties are estimated from Monte Carlo simulations. M97 and M01 measured the Compton y -parameter based on their Owens Valley 5.5 m data at 32 GHz. To compare the predicted y -parameter from our X-ray observations with their measured value, we correct for specifics of the 5.5 m telescope (the OVRO beam and the switching pattern; see eqs. [32]–[37] of M97 for details). After those corrections, we obtain a predicted y -parameter specific for the 5.5 m telescope: $(6.16 \pm 0.06) \times 10^{-5}$ (y_{pred} , 1σ error). The systematic errors from X-ray observations can further contribute up to 4% error (mainly from the uncertainties of temperatures). This value has a much smaller statistical uncertainty than the estimates in M97 and M01 [$(4.2 \pm 1.0) \times 10^{-5}$ and $(6.05 \pm 0.54) \times 10^{-5}$]. Moreover, our derivation of the Compton y -parameter is more accurate than the simple methods adopted in M97 and M01, which were limited by the X-ray data at that time.

We can use this result to obtain an estimate of H_0 . M01 obtained the observed y -parameter $(7.77 \pm 0.58) \times 10^{-5}$ (1σ error). However, after we examined the relativistic correction they used, which depends on the measured

temperature, we changed the relativistic correction factor to 1.026 following Itoh, Kohyama, & Nozawa (1998). Thus, the observed y -parameter should be $(7.71 \pm 0.57) \times 10^{-5}$ (y_{obs} , 1σ error). In principle, $h = (y_{\text{pred}}/y_{\text{obs}})^2$. Including the uncertainty from intrinsic CMB anisotropies (see details in M01), we obtain a Hubble constant $H = 64^{+32}_{-18}$ km s $^{-1}$ Mpc $^{-1}$ (1σ error). Intrinsic CMB anisotropies and the uncertainty of the radio observation are the main sources of the statistical uncertainties. Besides X-ray calibration uncertainties mentioned above, other systematic uncertainties include calibration uncertainties in the radio observations (3%—M01), uncertainty from peculiar motion (2% for 500 km s $^{-1}$ peculiar motion), clumping of X-ray gas ($\sim -15\%$), undetected radio sources ($\sim 10\%$), and unknown geometry ($\sim 10\%$ based on the analysis in Hughes & Birkinshaw 1998). A478 only serves as an example. As more SZE clusters are observed by *Chandra* and *XMM-Newton*, and as better radio observation are available, a systematic analysis will provide a better constraint on H_0 .

The results presented here are made possible by the successful effort of the entire *Chandra* team to build, launch, and operate the observatory. We acknowledge helpful discussions with L. David, D. Harris, M. Markevitch, and A. Vikhlinin. We thank the Smithsonian Institution for support. We thank the referee for comments. This study was also supported by NASA contract NAS8-38248.

REFERENCES

- Allen, S. W. 2000, *MNRAS*, 315, 269
 Allen, S. W., et al. 1993, *MNRAS*, 262, 901
 Anders, E., & Grevesse, N. 1989, *Geochim. Cosmochim. Acta*, 53, 197
 Bahcall, N. A., & Sargent, W. L. W. 1977, *ApJ*, 217, L19
 Blanton, E., Sarazin, C., McNamara, B. R., & Wise, M. W. 2001, *ApJ*, 558, L15
 Boehringer, H., Voges, W., Fabian, A. C., Edge, A. C., & Neumann, D. M. 1993, *MNRAS*, 264, L25
 Churazov, E., et al. 2001, *ApJ*, 554, 261
 David, L. P., et al. 2001, *ApJ*, 557, 546
 Edge, A. C. 2001, *MNRAS*, 328, 762
 Ekers, R. D., & Simkin, S. M. 1983, *ApJ*, 265, 85
 Fabian, A. C., et al. 2000, *MNRAS*, 318, L65
 ———. 2002, *MNRAS*, 331, 369
 Heinz, S., Choi, Y.-Y., Reynolds, C. S., & Begelman, M. C. 2002, *ApJ*, 569, L79
 Hughes, J. P., & Birkinshaw, M. 1998, *ApJ*, 501, 1
 Itoh, N., Kohyama, Y., & Nozawa, S. 1998, *ApJ*, 502, 7
 Johnstone, R. M., Fabian, A. C., Edge, A. C., & Thomas, P. A. 1992, *MNRAS*, 255, 431
 Markevitch, M., & Vikhlinin, A. 2001, *ApJ*, 563, 95
 Markevitch, M., et al. 2000, *ApJ*, 541, 542
 ———. 2003, *ApJ*, 583, 70
 Mason, B. S., Myers, S. T., & Readhead, A. C. S. 2001, *ApJ*, 555, L11 (M01)
 Maukopf, P. D., et al. 2000, *ApJ*, 538, 505
 McNamara, B. R., et al. 2000, *ApJ*, 534, L135
 ———. 2001, *ApJ*, 562, L149
 Myers, S. T., et al. 1997, *ApJ*, 485, 1 (M97)
 Plucinsky, P. P., et al. 2003, *Proc. SPIE*, in press (astro-ph/0209161)
 Reese, E. D., et al. 2000, *ApJ*, 533, 38
 Soker, N., Blanton, E., & Sarazin, C. 2002, *ApJ*, 573, 533
 White, D. A. 2000, *MNRAS*, 312, 663
 White, D. A., et al. 1994, *MNRAS*, 269, 589
 Zabludoff, A., Huchra, J., & Geller, M. 1990, *ApJS*, 74, 1
 Zhao, J. H., Sumi, D. M., Burns, J. O., & Duric, N. 1993, *ApJ*, 416, 51